# A quantum-mechanical study of the reaction mechanism of sulfite oxidase

**ARTICLE** *in* JBIC JOURNAL OF BIOLOGICAL INORGANIC CHEMISTRY · JUNE 2014

Impact Factor: 2.54 · DOI: 10.1007/s00775-014-1172-z · Source: PubMed



**7 AUTHORS**, INCLUDING:

Marie-Céline Van Severen
Lund University
**17** PUBLICATIONS **163** CITATIONS
SEE PROFILE

Jilai Li
Jilin University
**65** PUBLICATIONS **270** CITATIONS
SEE PROFILE

Ricardo A. Mata
Gesellschaft für wissenschaftliche Datenver…
**58** PUBLICATIONS **840** CITATIONS
SEE PROFILE

Ulf Ryde
Lund University
**219** PUBLICATIONS **7,472** CITATIONS
SEE PROFILE

J Biol Inorg Chem (2014) 19:1165–1179
DOI 10.1007/s00775-014-1172-z

ORIGINAL PAPER

# A quantum-mechanical study of the reaction mechanism of sulfite oxidase

**Marie-Céline van Severen · Milica Andrejić · Jilai Li · Kerstin Starke · Ricardo A. Mata · Ebbe Nordlander · Ulf Ryde**

Received: 6 December 2013 / Accepted: 5 June 2014 / Published online: 24 June 2014


**Abstract** The oxidation of sulfite to sulfate by two different models of the active site of sulfite oxidase has been studied. Both protonated and deprotonated substrates were tested. Geometries were optimized with density functional theory (TPSS/def2-SV(P)) and energies were calculated either with hybrid functionals and large basis sets (B3LYP/def2-TZVPD) including corrections for dispersion, solvation, and entropy, or with coupled-cluster theory (LCCSD(T0)) extrapolated toward a complete basis set. Three suggested reaction mechanisms have been compared and the results show that the lowest barriers are obtained for a mechanism where the substrate attacks a Mo-bound oxo ligand, directly forming a Mo-bound sulfate complex, which then dissociates into the products. Such a mechanism is more favorable than mechanisms involving a Mo–sulfite complex with the substrate coordinating either by the S or O atom. The activation energy is dominated by the Coulomb repulsion between the Mo complex and the substrate, which both have a negative charge of −1 or −2.

**Keywords** Molybdenum · Sulfite oxidase · Quantum mechanics · Density functional theory · Coupled-cluster calculations · CCSD(T)

## Introduction

Molybdenum is the most common transition metal in seawater, with a concentration that is 100 times higher than that of iron, for example [1]. Therefore, it is not unexpected that it is used in several enzymes. Two main groups of Mo enzymes are known. One is nitrogenase, which converts $N_2$ to $NH_3$ using a complicated $Fe_7S_9CMo$ cofactor [2]. The second is a large group of oxygen-transfer and hydroxylase enzymes that contain mononuclear molybdenum cofactors (collectively designated as Moco) that constitute the active sites of the enzymes. Over 50 Moco-dependent enzymes are currently known [3, 4], e.g. the aldehyde, sulfite, and xanthine oxidases. Since several Moco-dependent enzymes play essential roles in the carbon, nitrogen and sulfur cycles, such enzymes are found in all types of organisms, from archaebacteria to man. In all cases, the molybdenum atom of the cofactor is ligated by an organic molecule that is unique to mononuclear molybdenum (and related tungsten) enzymes, viz. molybdopterin, a bidentate ligand that coordinates to Mo through a dithiolene moiety (Fig. 1).

In this study, we focus on the mechanism of sulfite oxidases [5], which detoxifies sulfite by oxidizing it to sulfate [6]. This reaction is the terminal step in the biological sulfur cycle in many organisms, including man. Deficiency of this enzyme in man may lead to neurological

**Electronic supplementary material** The online version of this article (doi:10.1007/s00775-014-1172-z) contains supplementary material, which is available to authorized users.

M.-C. van Severen · J. Li · U. Ryde (✉)
Theoretical Chemistry, Department of Chemistry, Chemical Centre, Lund University, P. O. Box 124, 221 00, Lund, Sweden
e-mail: ulf.ryde@teokem.lu.se

M. Andrejić · R. A. Mata
Institut für Physikalische Chemie, Universität Göttingen, Tammannstrasse 6, 37077, Göttingen, Germany

J. Li
State Key Laboratory of Theoretical and Computational Chemistry, Institute of Theoretical Chemistry, Jilin University, Changchun 130023, People's Republic of China

K. Starke · E. Nordlander
Chemical Physics, Department of Chemistry, Chemical Centre, Lund University, P. O. Box 124, 221 00 Lund, Sweden

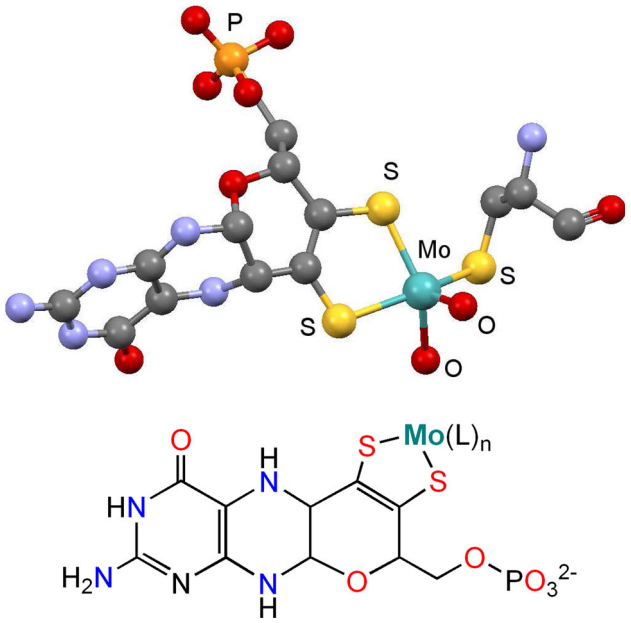


**Fig. 1** The minimal coordination unit of a molybdenum cofactor (Moco), as exemplified from the active site of sulfite oxidase (1SOX crystal structure [8]). In prokaryotic cofactors, a nucleotide (inosine monophosphate, adenosine monophosphate, or guanosine monophosphate) is bound to the phosphate group of the molybdopterin

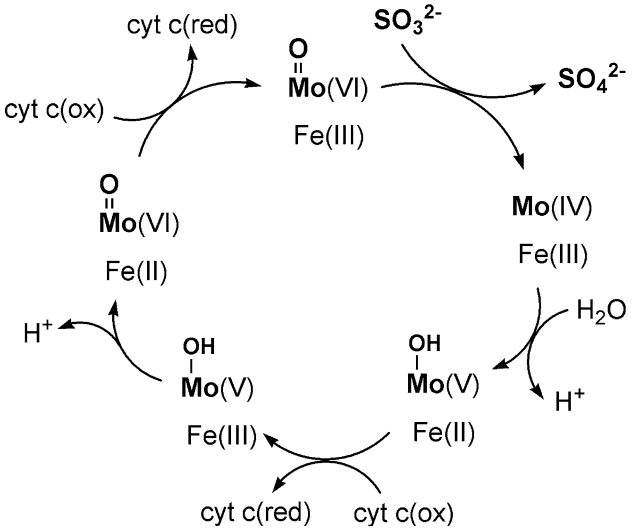


**Fig. 2** A general catalytic cycle for sulfite oxidase (adapted from [5]), the molybdenum ion refers to the molybdenum cofactor, and the iron ion refers to the heme

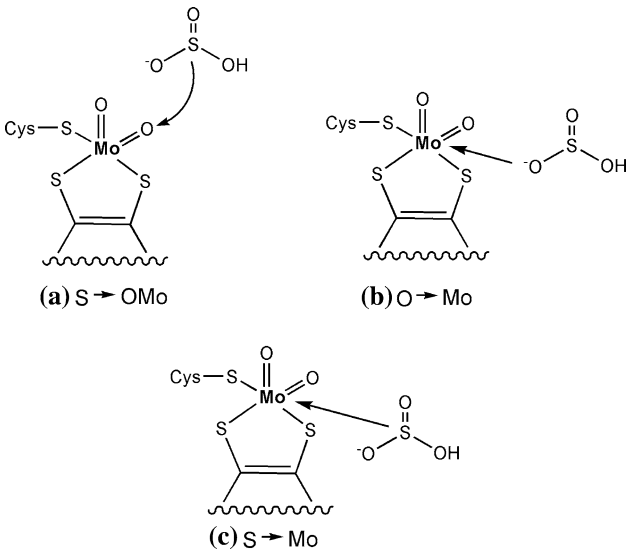


**Fig. 3** The three reaction mechanisms considered, **a** S→OMo mechanism, **b** O→Mo mechanism, and **c** S→Mo mechanism

problems, mental retardation, and dislocation of the ocular lens [7]. Crystal structures of both wild-type and mutant sulfite oxidases from several organisms have been determined [8–12]. The active site of the enzyme contains a molybdenum cofactor, which in its oxidized state contains a $Mo^{VI}$ ion that is bound to molybdopterin, two oxo ligands, and a cysteine residue from the protein (Fig. 1). The geometry is square pyramidal with one of the oxygen atoms in the axial position.

The enzyme also contains a heme group that is located ~30 Å from the Mo ion. At the start of the catalytic cycle (Fig. 2), Mo is in the oxidized +VI state and the heme group is in the Fe(III) state [5]. Then $SO_3^{2-}$ (or $HSO_3^-$) binds and is oxidized to $SO_4^{2-}$, while the Mo ion is reduced to the +IV state. To complete the catalytic cycle, the reduced Mo ion binds water and is reoxidized to the +VI state in two coupled one-electron/proton-transfer steps, proceeding via a transient Mo(V)–$OH^-$ state to form the active Mo(VI)=O form of the cofactor. The electrons are transferred via reduction of the heme (steps 2 and 4; Fig. 2), which subsequently is reoxidized by cytochrome *c* (steps 3 and 5). In this article, we focus on the first step of this catalytic cycle, i.e. the oxidation of $SO_3^{2-}$ to $SO_4^{2-}$.

Despite the apparent simplicity of the reaction, there has been considerable discussion regarding the molecular mechanism of the oxo-atom transfer. Three different mechanisms have been suggested, as shown in Fig. 3: One possibility is that the lone pair of the sulfur atom of $SO_3^{2-}$ attacks the equatorial oxygen of Mo (S→OMo mechanism), originally proposed by Hille [13, 14]. Indirect evidence for this mechanism includes the fact that the crystal structure of chicken liver sulfite oxidase [8] contains a molecule of the sulfate product, which is positioned in a way that suggests it is the product of an S→OMo mechanism. Another possibility is that one of the oxygen atoms of $SO_3^{2-}$ attacks Mo, forming a Mo–O bond (O→Mo mechanism). The third possibility is that the lone pair of S directly attacks Mo, forming a Mo–S bond (S→Mo mechanism).

The O→Mo mechanism was first proposed by Sarkar and coworkers. They showed that a molybdenum dithiolene model complex $[MoO_2(MNT)_2]^{2-}$ (MNT, maleonitrile dithiolate) is a functional model for sulfite oxidase that can oxidize $HSO_3^-$ to $HSO_4^-$ [15, 16]. The model complex exhibited Michaelis–Menten type of kinetic behavior [15, 17], which led these authors to propose that the mechanism of oxidation is different from that observed for oxygen-atom transfer by $Mo(VI)O_2$ model complexes to abiological oxygen acceptors, e.g. phosphines or phosphites [17]. For the latter type of reactions, no saturation behavior is observed and it is generally agreed that they occur via direct attack of the substrate at an oxo ligand of the molybdenum complex (corresponding to the S→OMo mechanism). In the case of the above-mentioned sulfite oxidase model system, it was proposed that the Michaelis complex of this reaction consists of $[MoO_2(MNT)_2(HSO_3)]^{3-}$, in which $HSO_3^-$ coordinates to Mo via one of the O atoms to form a seven-coordinate intermediate (i.e. the O→Mo mechanism) [18, 19]. Indirect evidence in support of such a mechanism was provided by an EXAFS investigation of arsenate-complexed reduced sulfite oxidase [20] which indicated that arsenate binds directly to the molybdenum atom via an As–O–Mo interaction. Furthermore, pulsed EPR studies on the phosphate-inhibited Mo(V) form of human sulfite oxidase have shown that phosphate binds terminally to the molybdenum atom [21, 22]. In addition, it should be noted that EPR/HYSCORE spectroscopy on the substrate- or product-inhibited low-pH reduced Mo(V) form of human sulfite oxidase with $^{33}S$-labeled sulfite is consistent with the coordination of a sulfite oxoanion to the metal ion, which was also modeled computationally [21, 22]. However, it should be noted that these experiments were performed on the R160Q mutant of the enzyme [23] and that the observed species should be considered as a dead-end species of the enzyme; thus, the detected coordination of sulfite in these specific experiments do not in themselves support an O→Mo mechanism.

The sulfite oxidation by model complexes and the corresponding oxidative half-reaction of sulfite oxidase have been computationally modeled by several groups. In a density functional theory (DFT) study, Thapper et al. [24] found that the S→OMo mechanism for $[MoO_2(MNT)_2]^{2-}$ is more favorable than the S→Mo mechanism. As the structure of the proposed $[MoO_2(MNT)_2(HSO_3)]^{3-}$ intermediate was not defined in the original publication [15], Thapper et al. interpreted this to implicate the S→Mo mechanism whereas the O→Mo mechanism was not tested. To our knowledge, the above-mentioned study was the first to discuss the possibility of an S→Mo mechanism.

In a related computational study, in which the sulfite oxidase active site was modeled by $[MoO_2(DMDT)(SCH_3)]^-$ (DMDT = 1,2-dimethyldithiolene), Kirk et al. [25] found that the two oxo ligands are distinctly different and that only the equatorial oxo ligand is reactive. More recently, Sarkar et al. [19, 26] published a DFT study of the oxidation of $HSO_3^-$ by both $[MoO_2(MNT)_2]^{2-}$ and $[MoO_2(DMDT)(SCH_3)]^-$, and concluded that the reaction proceeds via the O→Mo mechanism. Finally, Hernandez-Marin and Ziegler [27] used $[MoO_2(DMDT)(SCH_3)]^-$ extended with an arginine model ($CH_3NHC(NH_2)_2$) hydrogen-bonded to the equatorial oxo ligand to model sulfite oxidation. Their results supported the S→OMo mechanism.

In the present investigation, an attempt has been made to resolve these conflicting results by studying all the three reaction mechanisms with the same quantum mechanical (QM) methods and models. In line with the previous studies [19, 24, 25, 27], we use the QM cluster model approach that has been shown to be successful for many other enzyme reactions [28, 29]. In addition, we calibrate our results to coupled-cluster calculations, use large saturated basis sets, and include thermal, solvation and dispersion effects to improve the reaction energetics [30].

## Methods

The active site of sulfite oxidase was modeled by a Mo ion, coordinated to one or two oxo ligands, a cysteine ligand, modeled by $CH_3S^-$, the substrate, and molybdopterin. The latter group was modeled either as the complete ligand, besides the phosphate group that was replaced by a hydroxyl group (MPT; Fig. 4a), or by DMDT (Fig. 4b; the negative charge of the phosphate group may strongly affect the energetics of the reactions if included without compensating positively charged groups from the protein [31, 32]). The $pK_a$ value of $HSO_3^-$ is 7.2 [33]; therefore, we studied the reaction mechanism with both $HSO_3^-$ and $SO_3^{2-}$ as the substrate.

The QM geometry optimisations were performed at the density functional theory (DFT) level with the TPSS functional [34] and the def2-SV(P) basis sets [35], implying a relativistic 28-electron effective core potential for Mo. The calculations were sped up by expanding the Coulomb interactions in the corresponding def2-SV(P) auxiliary basis sets, the resolution-of-identity (RI)

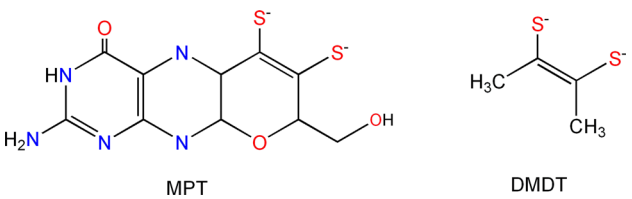


**Fig. 4** The two models used for the molybdopterin cofactor in this paper, MPT and DMDT

approximation [36, 37]. For each optimized structure, a frequency calculation was performed at the same level of theory to ensure that a proper stationary structure or saddle point was obtained. These frequency calculations also permitted calculation of zero-point vibrational energies and thermal corrections to the Gibbs free energy, obtained by a rigid-rotor harmonic-oscillator ideal-gas approximation at 298 K and 1 atm pressure. Single-point energy calculations were performed with the larger def2-TZVPD basis set [35, 38] at the B3LYP level [39, 40] to estimate the effect of the basis set and the DFT functional. Test calculations showed that diffuse functions were needed to obtain converged energies (see Discussion in the supplementary material); with the current basis set, the calculations reproduce energies calculated with the even larger def2-QZVPPD basis set within 4 kJ/mol, whereas calculations without the diffuse functions (i.e. def2-TZVP) differed by 22–77 kJ/mol from the def2-QZVPPD results.

Environmental effects were incorporated by single-point calculations in a continuum solvent with different dielectric constants, $\varepsilon = 4$ or 80, using the COSMO approach with optimized radii (and 2.0 Å for Mo) [41–43]. These calculations were also performed at the B3LYP/def2-TZVPD level. Together with the vacuum results ($\varepsilon = 1$), they should include possible effects in the enzyme, for which the dielectric constant is usually assumed to be between 2 and 20 [44, 45]. All DFT calculations were performed with the Turbomole software [46].

Dispersion effects were calculated by single-point calculations using the DFT-D3 method [47], obtained with the dftd3 program for the B3LYP functional with default parameters [48]. In addition, continuum estimates of the cavitation, dispersion, and repulsion energies for all complexes with the surroundings were estimated with the polarized continuum method (PCM) [49, 50], as implemented in the Gaussian03 software [51]. These calculations used the UAKS radii (united atom topological model for Kohn–Sham theory). The non-polar solvation energies are needed to obtain a balance in the solvation and dispersion energy terms for reactions in which a ligand binds or dissociates to a metal complex [52]. We assumed that the active-site cavity of sulfite oxidase does not change during the reaction (i.e. that the active site is preformed and that its shape and volume do not change significantly during the reaction). Therefore, we ignored the cavitation term for the enzyme models (i.e. the molecules involving DMDT or MPT), but not for the substrates and products ($HSO_3^-$, $HSO_4^-$, $H_2O$, etc) [30, 52]. Such an approximation seems to be reasonable for the hidden active site of sulfite oxidase and reduces the energies of all intermediates and transition states of the reaction by ~46 kJ/mol. The various corrections are listed in Table S2 in the supplementary material.

To check the consistency of the results, we also performed some geometry optimisations at the B3LYP/def2-TZVPD level in the COSMO solvent with a dielectric constant of 80 and DFT-D3 dispersion. Only selected structures were studied and the transition states were obtained by scanning two bond lengths (Mo–O and S–O).

Finally, we have carried out local second-order Møller–Plesset perturbation theory (LMP2) [53], spin-component-scaled (SCS) LMP2, and local coupled-cluster calculations with singles, doubles and non-iterated perturbative triples (LCCSD(T0)) [54] on all DMDT complexes. Two sets of orbital basis functions were used. In the first, referred to as AVTZ, the aug-cc-pVTZ basis set [55] was used for all elements, except H (cc-pVTZ [56]) and Mo (aug-cc-pVTZ-PP with the Stuttgart–Dresden ECP28MDF pseudopotential [57]). The second was an analogous quadruple-zeta basis set (AVQZ: cc-pVQZ for H, aug-cc-pVQZ-PP for Mo with the corresponding pseudopotential, and aug-cc-pVQZ on the other atoms). Density-fitting (DF) approximations [58, 59] were used for both the Hartree–Fock and the correlation part. The auxiliary basis sets were aug-cc-pV*n*Z/JKFIT [60] and aug-cc-pV*n*Z/MP2FIT [61] for all elements except Mo for which the def2-*n*ZVPP/JKFIT [62] and def2-*n*ZVPP/MP2FIT [63] basis sets were applied ($n = T, Q$). Localized Pipek–Mezey orbitals [64] were used and the orbital domains were determined according to a natural population analysis occupation threshold of $T_{\mathrm{NPA}} = 0.03$ [65]. The orbital pairs were classified according to mixed distance and connectivity criteria. Further details are given in the supplementary material. All calculations were carried out with a development version of Molpro 2012.1 [66].

To account for basis-set incompleteness effects, the DF-LCCSD(T0)/AVTZ energies were corrected by estimating the canonical MP2 complete basis-set limit (CBS). Calculations at the DF-MP2/AVTZ and DF-MP2/AVQZ levels of theory were carried out. An $n^{-3}$ extrapolation of the correlation energy was performed from the two points [67] (MP2/CBS[3:4]) and added to the HF/AVQZ reference energy. The final composite energy, including higher order correlation effects from the local coupled-cluster result and the CBS extrapolation was computed from:

$$E(\mathrm{CC/CBS}) = E(\mathrm{LCCSD(T0)/AVTZ}) - E(\mathrm{LMP2/AVTZ}) + E(\mathrm{MP2/CBS[3:4]}). \quad (1)$$

The results of all these calculations are described in Table S2 in the supplementary material. It can be seen that LCCSD(T0) increases all energies (compared to the B3LYP-D3/def2-TZVPD calculations) by 2–62 kJ/mol (27 kJ/mol on average).

The presented energies are obtained by the following equation:

$$\Delta G_{\text{tot}} = \Delta E(\text{QM}) + \Delta G(\text{PCM}) + \Delta G(\text{therm}) + \Delta G(\text{solv}, \epsilon), \quad (2)$$

where $\Delta G$(solv,ε) is the solvation energy (the energy difference between the COSMO calculations with dielectric constants of ε and 1), $\Delta G$(therm) is the thermal correction to the Gibbs free energy (from the frequency calculations, including the zero-point energy), $\Delta G$(PCM) is the sum of the PCM cavitation, dispersion and repulsion energies, whereas $\Delta E$(QM) is the LCCSD(T0)/CBS energy in Eq. (1) for the DMDT models, but

$$\Delta E(\text{QM}) = \Delta E_{\text{MPT}}(\text{B3LYP-D3}) + \Delta E_{\text{DMDT}}(\text{CC/CBS}) - \Delta E_{\text{DMDT}}(\text{B3LYP-D3}), \quad (3)$$

where $\Delta E$(B3LYP-D3) is the sum of the B3LYP/def2-TZVPD and DFT-D3 energies and the subscript indicates which model was used (MPT or DMDT), i.e. the MPT energies were improved by the LCCSD(T0)/CBS correction from the corresponding DMDT complex. We will discuss four different energies: $\Delta G_4$ and $\Delta G_{80}$ are free energies in continuum solvents with dielectric constants of 4 or 80, respectively, obtained from Eq. (2), $\Delta G_1$ is the free energy without any solvation (i.e. $\Delta G(\text{solv},1) = 0$ in Eq. 2), and $\Delta E$ is the vacuum energy without any thermal corrections (i.e. with $\Delta G(\text{therm}) = \Delta G(\text{solv},1) = 0$ in Eq. 2).

## Results and discussion

In this paper, we present a QM cluster model study of the oxo transfer mediated by the cofactor of sulfite oxidase, using either $HSO_3^-$ or $SO_3^{2-}$ as substrates (both are substrates for sulfite oxidase under physiological conditions). The results for two enzyme models (with either DMDT or MPT) are given. The results for the three suggested mechanisms (S→OMo, O→Mo, and S→Mo) are discussed in separate sections.

### S→OMo mechanism

The reaction path in which the sulfur atom of the substrate attacks the equatorial oxo ligand ($O_{eq}$) of molybdenum (Fig. 3) was studied first. Previous calculations have indicated that only the equatorial oxide was reactive in this mechanism [25]. Test calculations involving instead the axial ligand showed that the complex reorganized so that the reacting oxo ligand became equatorial. Therefore, results are only presented for reactions with the equatorial oxo ligand. The reactions were studied with both DMDT and MPT as models of the molybdopterin ligand, and with both $HSO_3^-$ and $SO_3^{2-}$ as the substrate. For clarity, only structures with DMDT and $HSO_3^-$ are shown in the figures, but the results for MPT and $SO_3^{2-}$ are similar. On the other hand, geometric and energetic results are only presented for the MPT ligand, whereas the corresponding results for the DMDT ligand can be found in the supplementary material.

The investigation was started from the reactant state (RS) with the oxidized active site without any substrate (Fig. 5). When sulfite attacks this complex, an intermediate with sulfate coordinated to Mo(IV) is formed (IM1), via a transition state (TS1). Thus, the chemical reaction takes place already at this step, as is confirmed by an analysis of the molecular orbitals. Next, sulfate dissociates from the molybdenum complex via a second transition state, TS2, giving rise to a four-coordinate product state, PS. For the reduced state of the Mo complex, we have also studied a structure in which a water ligand replaces the product, keeping the Mo complex five-coordinate (PW), in agreement with crystal structures of the product [8]. All these structures are shown in Fig. 5.

The Mo–X distances of these six complexes with the $HSO_3^-$ substrate are shown in Fig. 6. It can be seen that the Mo–$O_{eq}$ distance increases during the reaction. This is expected, because it changes from a Mo=O oxide ligand to a singly bonded sulfate group. It is 1.74 Å in RS, 1.91 Å in TS1, 2.21 Å in IM1, and 4.00 Å in TS2. In PS, the $HSO_4^-$ group has dissociated and in PW, it has been replaced by a water ligand with a Mo–O distance of 2.27 Å. On the other hand, the Mo–$O_{ax}$ distance hardly changes during the reaction (1.71–1.75 Å), indicating that this ligand is a spectator. The distances between Mo and MPT (Mo–$S_1$ and Mo–$S_2$) decrease when IM1 is formed (from 2.49 and 2.52 to 2.42 and 2.41 Å), probably as an effect of the elongated Mo–$O_{eq}$ distance, but partly counteracted by the reduction of the Mo ion and the increased negative charge of the complex. These bond lengths are further contracted when the product dissociates (to 2.34 and 2.35 Å), reflecting the decreased coordination number and net charge. They increase again when $H_2O$ binds, to 2.41 and 2.37 Å. The Mo–$S_{Cys}$ bond shows a similar behavior, varying between 2.37 and 2.45 Å.

The results for the $SO_3^{2-}$ substrate are shown in Fig. 6b. It can be seen that the bond lengths are similar, except that the Mo–$O_{eq}$ distances in TS1, IM1, and TS2 are 0.1–0.2 Å shorter with $SO_3^{2-}$ (with its doubly negative charge). Consequently, the three Mo–S bonds are longer when $SO_3^{2-}$ is the substrate. Moreover, the $O_{eq}$–$S_{Sub}$ ($S_{Sub}$ is the sulfur atom of the substrate) bond that is being formed in TS1 is much longer for $SO_3^{2-}$ (2.66 Å) than for $HSO_3^-$ (1.97 Å), indicating a later transition state for $HSO_3^-$, which is stabilized by a hydrogen bond between the substrate and the $O_{ax}$ ligand.

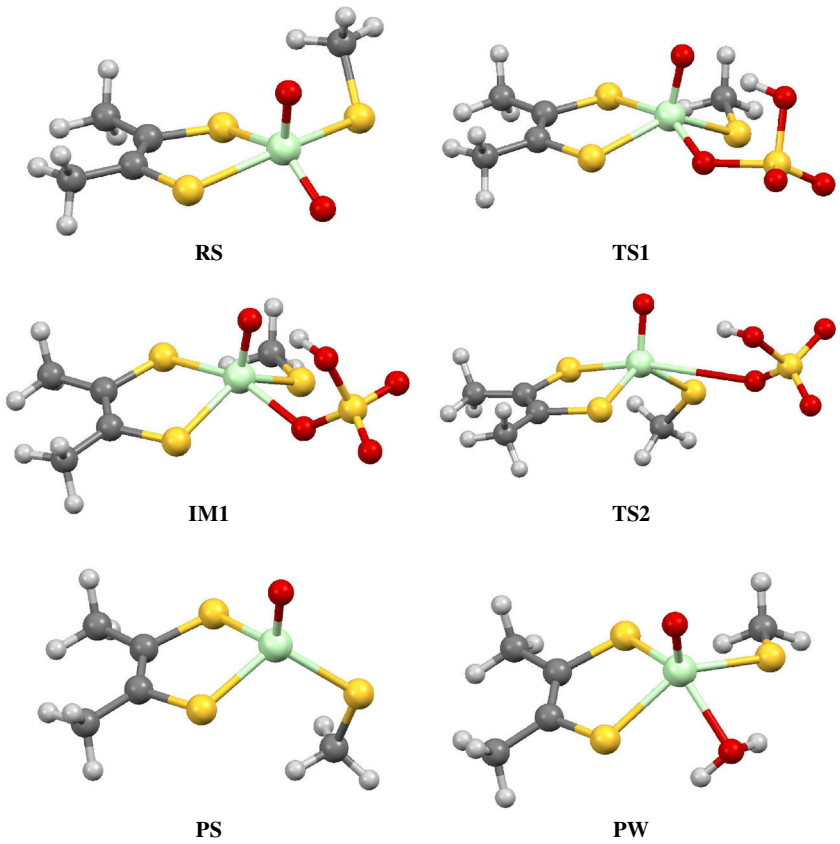


**Fig. 5** Optimized structures for the S→OMo mechanism of the sulfite-oxidase models. For clarity, structures with DMDT are shown, but the structures with MPT are closely similar, as are complexes with $SO_3^{2-}$ instead of $HSO_3^-$

In Fig. 6a, the results of previous DFT calculations on the PW state [19, 27] are also included, as well as the distances found in the crystal structure of sulfite oxidase from chicken liver [8] and in an EXAFS investigation of the reduced state of the human enzyme [68]. It can be seen that our calculations reproduce all the experimental distances within 0.04 (crystal) or 0.06 Å (EXAFS). This is better than in the previous investigations [19, 27], in which the Mo–$O_{Wat}$ distance was either 2.41 or 2.18 Å, differing by 0.09–0.14 Å both from the present result and from the experimental estimates. This difference is probably caused by differences in the DFT functional, basis sets, and molybdopterin model (the previous studies used the B3LYP or Becke–Perdew-1986 methods, a DMDT ligand, and somewhat different basis sets). The good agreement between our calculations and the experimental values shows that our calculations are reliable.

The energy profiles of the various reactants are shown in Fig. 7. Four energies are presented, viz. the energy in vacuum ($\Delta E$), and the free energies (calculated from the vibrational frequencies) in vacuum and in continuum solvents with dielectric constants of 4 and 80 ($\Delta G_1$, $\Delta G_4$, and $\Delta G_{80}$). As described in the "Methods" section (Eq. 2), the energies were obtained with the B3LYP method and the large def2-TVZPPD basis set. They include corrections for dispersion (both continuum-solvation and correction for the DFT functional), cavitation, and repulsion. In addition, the energies are corrected for deficiencies in the DFT method with the help of LCCSD(T0) calculations. The sum of the energies of the RS complex and the free substrate was taken as a reference.

It can be seen that the $\Delta E$ and $\Delta G_1$ results are similar, demonstrating that the thermal effects are small for this reaction, besides an entropic effect of binding a free ligand ($HSO_3^-$, $HSO_4^-$, or $H_2O$) of ~55 kJ/mol, favoring the dissociated states (RS and PS). As has been discussed before [69–71], this is probably an overestimate by ~30 kJ/mol. On the other hand, solvation effects are large, strongly reducing the activation barriers and the energy of the intermediate. The reason for this is that the active site of sulfite oxidase has a net charge of −1 in the RS, PS, and PW states. Likewise, both the substrate and the product have a net charge of −1 or −2, depending on whether they are protonated or not. Therefore, the reaction energies are dominated by the Coulomb repulsion between the complex and the substrate or products. Consequently, the activation energies and the energy of the intermediate are lowest in aqueous solution. However, the first activation free energy (of TS1) is still considerable, 159 kJ/mol for $HSO_3^-$. This means that the reaction in aqueous solution would be slow.

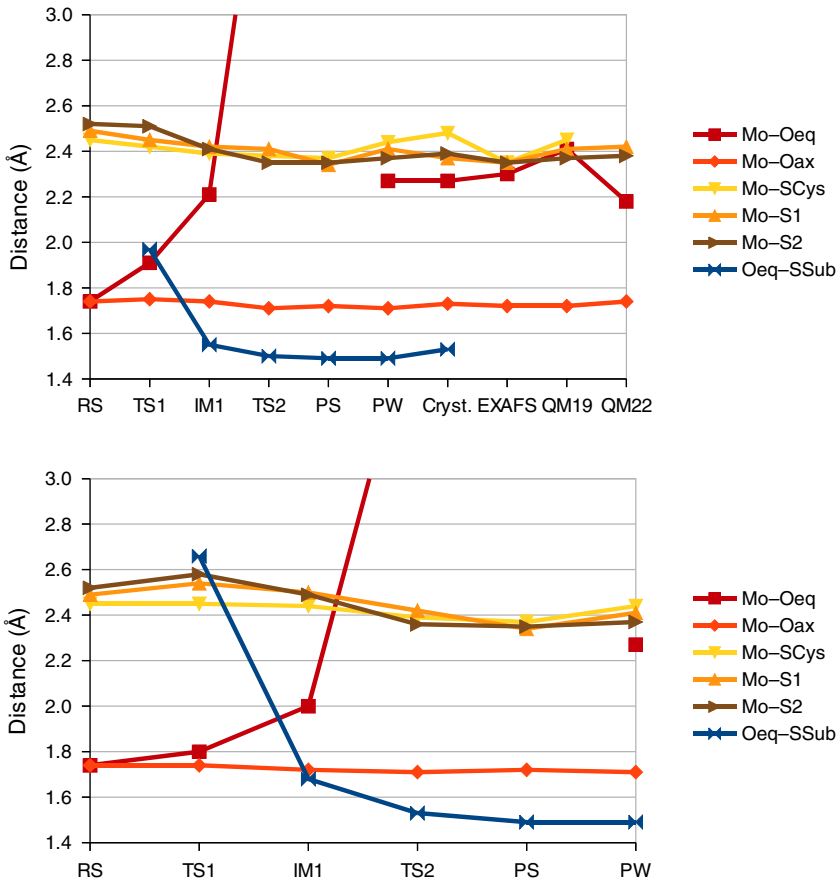


**Fig. 6** Bond lengths (Å) for the various states of the S→OMo mechanism with the MPT ligand and the **a** $HSO_3^-$ or **b** $SO_3^{2-}$ substrate. $S_1$ and $S_2$ are the two sulfur atoms of the MPT ligand ($S_1$ is cis to $O_{eq}$, whereas $S_2$ is cis to $S_{Cys}$). For the PW state in **a**, the results of previous QM calculations [19, 27], as well as of crystallographic (average of two subunits) [8] and EXAFS experiments [68] are also included

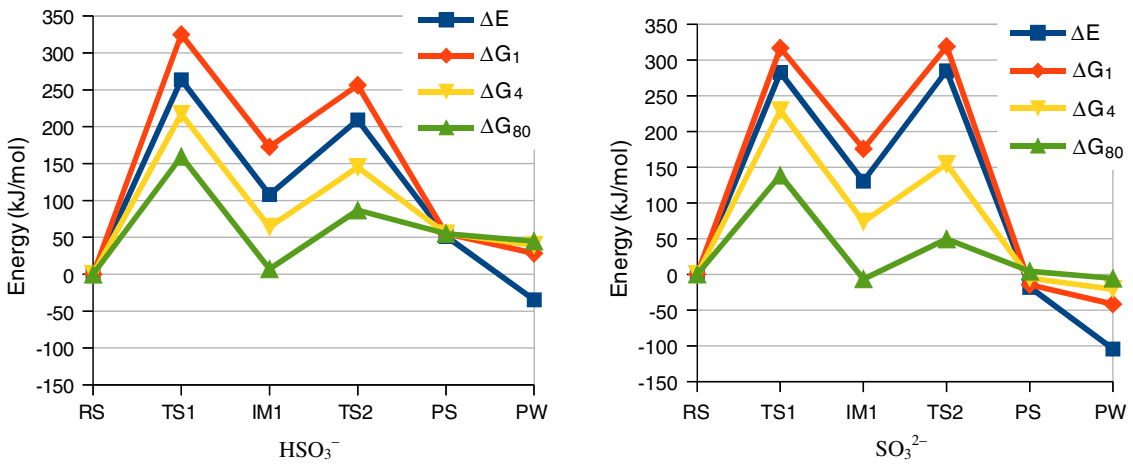


**Fig. 7** Energy profiles for the various reactants in the S→OMo mechanism with MPT (kJ/mol)

The intermediate is 7 kJ/mol higher in energy than the isolated reactants ($\Delta G_{80}$). The second transition state (TS2) is appreciably lower in energy than TS1 (87 kJ/mol). The dissociated product state (PS) is 55 kJ/mol higher in energy than RS. The binding of a water molecule is predicted to be exergonic by 10 kJ/mol.

The energies change somewhat with the $SO_3^{2-}$ substrate. The initial transition state, TS1, is still highest in energy with an activation energy of 139 kJ/mol in a water-like continuum solvent, i.e. 20 kJ/mol lower than with $HSO_3^-$. IM1 is also stabilized by 14 kJ/mol, whereas TS2 and the product states are stabilized even more, by 37 and 50 kJ/mol, respectively.

We have performed similar calculations with the truncated DMDT model of the molybdopterin ligand. The results are presented in Table S3 (geometries) and Figure S1 (energies). It can be seen that the geometries are similar to those obtained with the MPT model for both the protonated and deprotonated substrate (average difference 0.02 Å for the distances in Fig. 6; maximum differences up to 0.07 Å, except for TS2, for which the long dissociating Mo–$O_{eq}$ distance differs by 0.10–0.21 Å). For the energies, the differences are somewhat larger, especially in vacuum (up to 34 kJ/mol for $HSO_3^-$ and 85 kJ/mol for $SO_3^{2-}$). However, the qualitative results are still the same: The highest barrier is obtained for TS1 and it is lower for $SO_4^{2-}$ than for $HSO_4^-$. The lowest barrier, 107 kJ/mol, is obtained in a water-like solvent and a deprotonated substrate.

For all structures in the reaction mechanism, there are several possible conformations. We have restricted our investigations to structures resembling the crystal structure of sulfite oxidase [8–12], i.e. a structure with $Mo^{VI}$ bound to two oxo ligands, cysteine, and molybdopterin in a square-pyramidal geometry, with the axial oxo ligand directed upwards, the Cys model ($CH_3S^-$) directed backwards with the $S_{Cys}$–$C_{Cys}$ bond pointing toward the MPT ligand (the orientation is shown in Fig. 1). No constraints were used in the calculations and therefore the conformation was found to change somewhat for some intermediates or transition states. Still, considerable care has been taken to ensure that all reactants are connected throughout the reaction mechanisms.

To estimate the effect of restrictions in the geometry caused by the surrounding protein, we have reoptimized the structures of the six states in Fig. 5 with the $C_{Cys}$–$S_{Cys}$–Mo–S1 dihedral angle fixed to 37°, the value found in the A subunit of the crystal structure in Reference [8] (it was 35° in the other subunit). This increased the energies by 0–4 kJ/mol for RS, TS1, and IM1, by 7 kJ/mol for TS2, 11 kJ/mol for PW, and 34 kJ/mol for PS (Table S4). Thus, the geometric restrains have a minimal effect for the rate-limiting activation barrier of TS1, whereas they have a sizeable effect for the reaction energy, owing to the reduced coordination number of PS (this could have been anticipated already from the change in structure, seen in Fig. 5).

## O→Mo mechanism

Next, we investigated the second reaction mechanism, in which an oxygen atom of the substrate attacks Mo. This mechanism has been studied by Sarkar and coworkers [19], who suggested a simple mechanism involving two intermediates (a $Mo^{VI}$–$OSO_2H^-$ complex and a $Mo^{IV}$–$OSO_3H^-$ intermediate closely similar to our IM1 complex) and three transition states. However, we could not find any such path that is properly connected. The first intermediate computed by Sarkar and coworkers involves a Mo–$O_{Sub}$ bond, as is required for an O→Mo mechanism, but in the following transition state, this bond is broken. In fact, this transition state seems to be identical to our TS1, i.e. the rate-limiting transition state of the S→OMo mechanism. Thus, Sarkar and coworkers have not obtained a proper O→Mo mechanism, which we find to be appreciably more intricate, as is shown in Fig. 8.

The reaction starts with the same reactant state (RS) as in the S→OMo mechanism. Then, $HSO_3^-$ approaches and forms a six-coordinate $Mo^{VI}$–$HSO_3^-$ complex with a Mo–$O_{Sub}$ bond (IM2) via a transition state TS3. These two states were also obtained by Sarkar and coworkers [19]. However, the next step is a proton transfer from $HSO_3^-$ to the $O_{ax}$, giving a Mo(OH)($SO_3$) complex (IM2H) via transition state TS4. Next, the sulfur atom of $SO_3^{2-}$ can attack the equatorial oxo ligand, giving rise to a six-coordinate Mo complex, involving a bidentate sulfate ligand, IM3. It is formed via TS5, which represents the actual chemical step when sulfate is formed and Mo reduced to $Mo^{IV}$. Note that throughout these steps, the Mo–$O_{Sub}$ bond is intact. It is not until the next step that one of the two ligating atoms in $HSO_4^-$ dissociates from the Mo ion. At the same time, the proton is transferred back to the sulfate groups so that the product is the same intermediate, IM1, as in the S→OMo mechanism (via TS6). Finally, the product can dissociate in the same way as in the S→OMo mechanism (via TS2). If the substrate is $SO_3^{2-}$ instead, no proton transfers are needed, so the mechanism is simplified by omitting the IM2H and TS4 states.

Figure 9 shows the Mo-ligand distances for all the reactants with the MPT model. It can be seen that the Mo–$O_{eq}$ distance is constant at 1.74 Å (1.75–1.76 Å with $SO_3^{2-}$) during the first part of the reaction (RS→IM2H). After that, it first elongates as the sulfate group is formed, to 2.22 Å for $HSO_4^-$ and 2.11 Å for $SO_4^{2-}$, and then dissociates in TS2. The Mo–$O_{ax}$ distance does not change during the reaction (1.71–1.80 Å), except for the states with the $HSO_3^-$ when it becomes a protonated $OH^-$ ion (IM2H–IM3 1.91–1.95 Å). The Mo–$O_{Sub}$ bond, formed in IM2, is longer than for the oxy groups, but shorter than the bonds to $S_1$, $S_2$, and $S_{Cys}$. It is appreciably shorter for $SO_3^{2-}$ (1.88 Å) than for $HSO_3^-$ (2.08 Å). In the bidentate sulfate complex (IM3), it is even longer (2.22–2.28 Å) and in IM1, it has dissociated. The three Mo–S bonds are long in the six-coordinate complexes (2.5–2.8 Å), except in IM3 with $HSO_3^-$. For the five-coordinate complexes, they are ~2.4 Å.

The relative energies of the various reactants for the O→Mo mechanism are shown in Fig. 10. It can be seen that, also for this reaction, the energies depend strongly on solvent effects, which decrease the relative energies for all

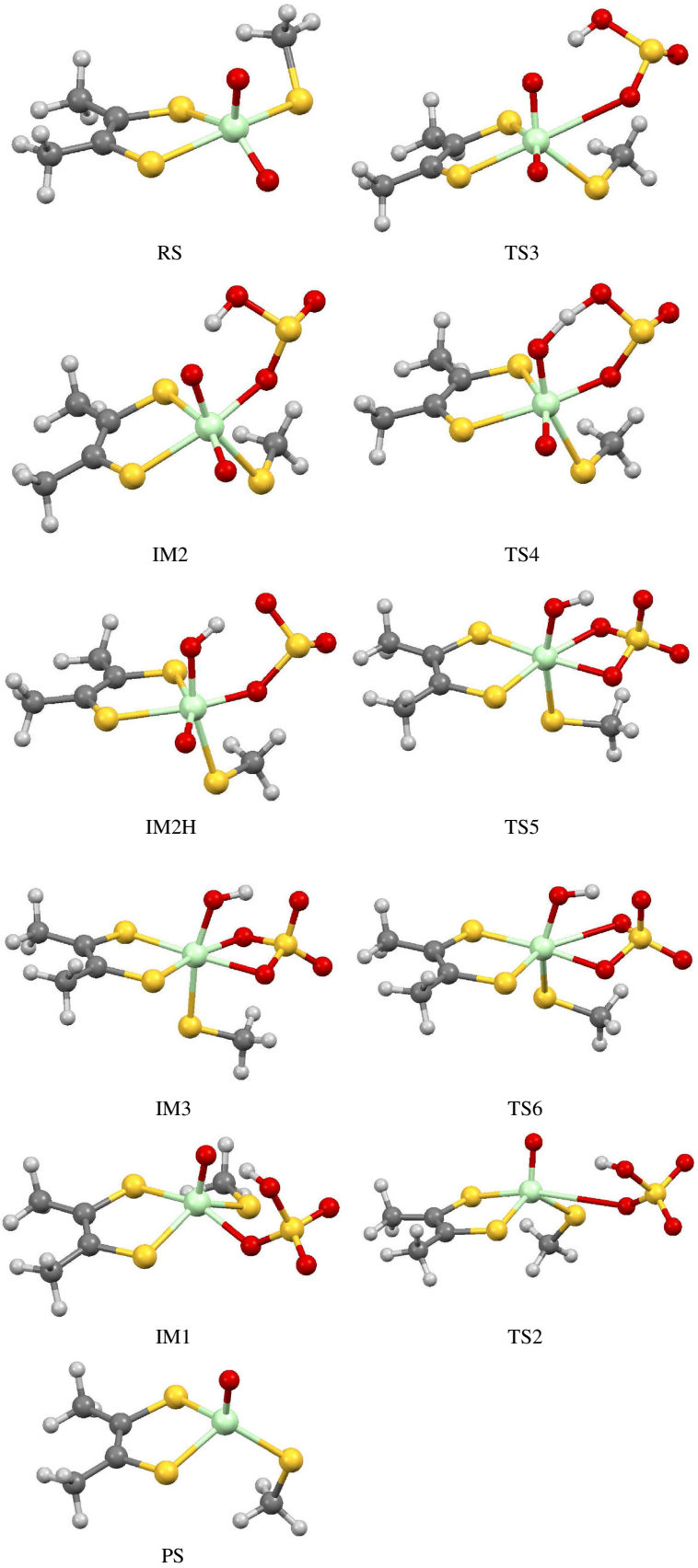


**Fig. 8** Optimized structures for the O→Mo mechanism with DMDT and $HSO_3^-$

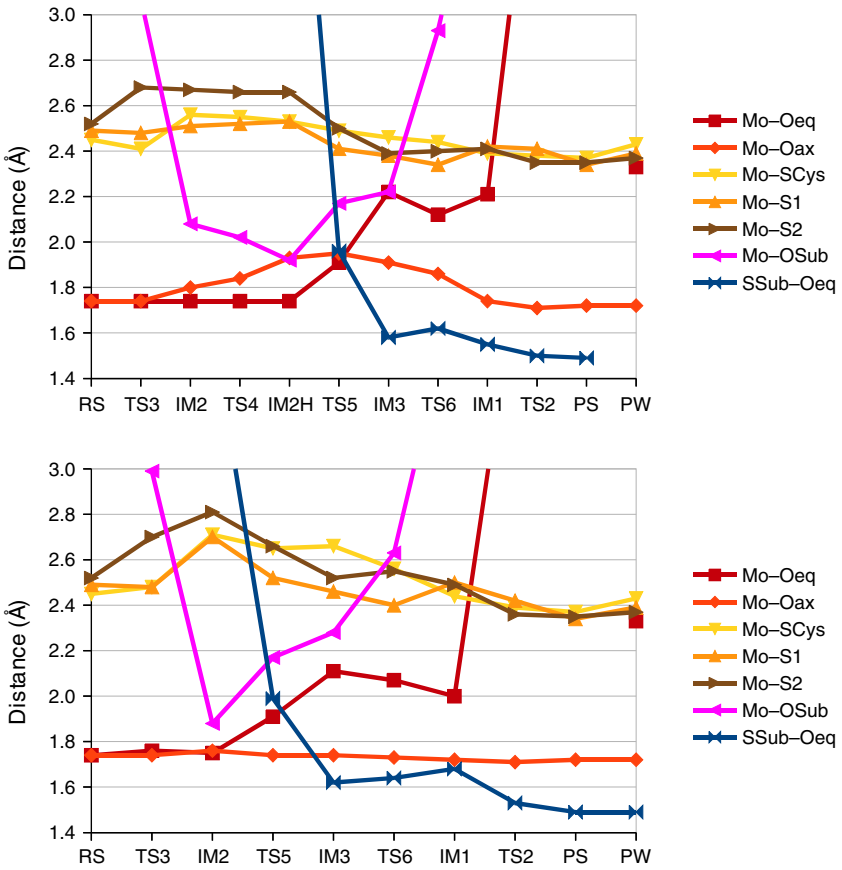


**Fig. 9** Bond lengths (Å) for the reactants in the O→Mo mechanism with the MPT group and the **a** $HSO_3^-$ or **b** $SO_3^{2-}$ substrate. $S_1$ and $S_2$ are the two sulfur atoms of the MPT group ($S_1$ is cis to $O_{eq}$, whereas $S_2$ is cis to $S_{Cys}$)

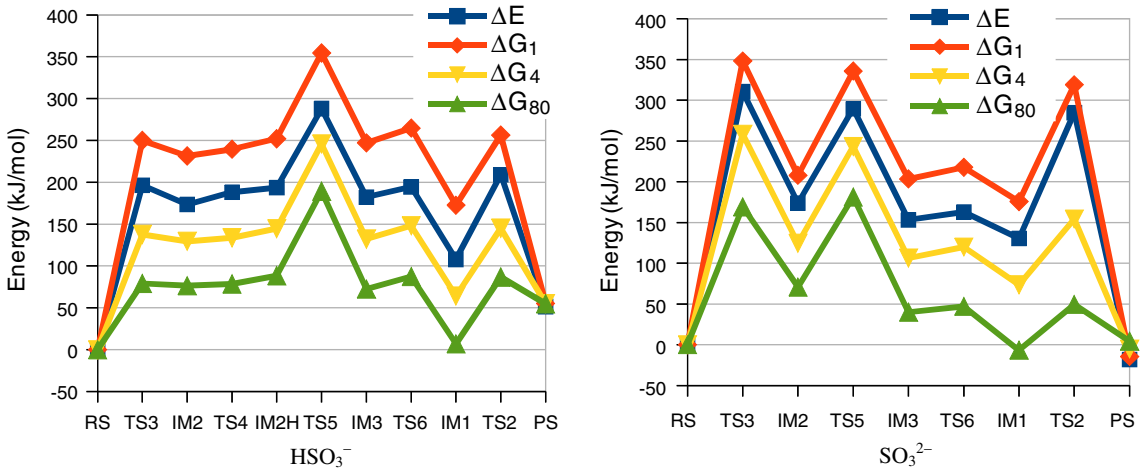


**Fig. 10** Energies for the O→Mo mechanism with MPT and $HSO_3^-$ (*left*) or $SO_3^{2-}$ (*right*; kJ/mol)

intermediates and transition states. The entropic and thermal effects increase the energies for intermediates and transition states.

For the O→Mo mechanism, there are large differences between the two substrates. For $HSO_3^-$, TS3 is quite low in energy, e.g. 79 kJ/mol in $\varepsilon = 80$, and IM2, TS4, IM2H, IM3, TS6, and TS2 have similar energies 72–88 kJ/mol. On the other hand, TS5 is much higher in energy, 189 kJ/mol, and IM1 is appreciably lower (7 kJ/mol). Consequently, the rate-limiting step is TS5, the formation of the S–O bond and the bidentate binding of the substrate. The activation energy for this step is 30 kJ/mol higher than that of TS1, the highest state in the S→OMo mechanism, making this mechanism less likely.

For $SO_3^{2-}$, the energies are more varying. TS5 is still high in energy (181 kJ/mol in water), but TS3 is also rather high (169 kJ/mol). Apparently, the hydrogen atom in $HSO_3^-$ strongly facilitates the formation of the first Mo–O bond by forming a hydrogen bond with the $O_{ax}$ atom, lowering the energy of TS3 by 90 kJ/mol. It is notable that also with $SO_3^{2-}$, the O→Mo mechanism is less favorable than the S→OMo mechanism, by 42 kJ/mol.

With the DMDT model of the molybdopterin ligand, the general shape of the energy diagrams (Fig. S2) is similar to those obtained with MPT. DMDT gives somewhat higher barriers in vacuum, but in the water-like continuum solvent they are typically slightly lower, with differences of up to 28 kJ/mol between DMDT and MPT. The transition state TS5 still gives the largest barrier for both substrates, with energies of 209 and 164 kJ/mol in the water-like continuum solvent. These energies are 50–57 kJ/mol higher than for the S→OMo mechanism. The geometries are also similar with differences of less than 0.09 Å for the bonds to Mo (Table S5).

Comparing the results discussed above to those obtained by Sarkar and coworkers, it may be noted that these authors obtained states that correspond to RS, TS3, IM2, TS1, IM1 and PW in our calculations, but they did not include the proton transfer to the spectator oxygen or the bidentate IM3 state and the rate-limiting transition state leading to it. We can conclude that our calculations indicate that the O→Mo mechanism is less favorable than the S→OMo mechanism. This is not an unexpected result, considering that the O→Mo mechanism is appreciably more complicated, including more reaction steps than the simple S→OMo mechanism, and that the two mechanisms share the IM1 and TS2 states. However, it is conceivable that several reaction steps are needed to avoid TS1, which is the highest transition state in the S→OMo mechanism.

Another argument also speaks against the O→Mo mechanism in the sulfite oxidase enzyme: As can be seen in Fig. 8, IM3 is almost symmetric with the methyl group of the Cys model located under the sulfate ligand. For most of the other intermediates and transition states, there are many possible conformations of the Cys model, but for IM3, we have only been able to find this conformation. Interestingly, this conformation deviates significantly from the conformation of the Cys ligand found in sulfite oxidase, in which the methyl group is pointing backwards and to the left, as in RS in Fig. 8. Therefore, it is unlikely that a stable IM3 can be found in the enzyme—on the contrary, the enzyme seems to be constructed to avoid the formation of such an intermediate. In fact, it is likely that even the complicated reaction mechanism in Fig. 8 would require additional steps if the conversions of the conformations of the Cys model are taken into account, but these conformations are close in energy.

### S→Mo mechanism

Finally, we also investigated the third mechanism, in which the lone pair of the S atom of the substrate attacks Mo. This mechanism involves an intermediate IM4, which is six-coordinate with the substrate bound to Mo by the S atom, as well as the corresponding transition state, TS7, for its formation (Fig. 11). However, a further reaction pathway beyond IM4 could not be fully elucidated. A decrease of the $O_{eq}$–$S_{Sub}$ distance typically led to cleavage of the Mo–$S_{Sub}$ bond before the $O_{eq}$–$S_{Sub}$ bond was formed, so that the transition state became similar to TS1 and the resulting intermediate was simply IM1 of the S→OMo mechanism. In the following, we have obtained an approximate TS8 by a two-dimensional scan of the Mo–$O_{eq}$ and $O_{eq}$–$S_{Sub}$ bonds, requiring an intact Mo–$S_{Sub}$ bond. As can be seen in Fig. 11, once IM1 is formed, the mechanism continues with the transition state TS2 to PS as in the other two mechanisms.

The Mo-ligand distances for the various states are shown in Fig. 12 for the MPT model. It can be seen that IM4 has a Mo–$S_{Sub}$ bond length of 2.77 ($HSO_3^-$) or 2.68 Å ($SO_3^{2-}$), i.e. longer than most of the Mo–$S_{Cys}$ and Mo–$S_{MPT}$ distances, indicating that the bond is weak. In TS7 it is 3.40 or 3.93 Å, respectively. In TS8, it is similar to that in IM4 (2.67 Å), whereas the $S_{Sub}$–$O_{eq}$ distance is 2.0–2.3 Å, and the Mo–$O_{eq}$ distance is 1.9 Å.

Figure 13 shows the energetics for the S→Mo mechanism. It can be seen that for both the protonated and deprotonated substrate, the activation barrier is very high, 274 kJ/mol for $HSO_3^-$ and 205 kJ/mol for $SO_3^{2-}$. This is 66–115 kJ/mol higher than for the S→OMo mechanism. Therefore, we can conclude that the S→Mo mechanism is unfavorable and can be disregarded. The corresponding DMDT results (Table S6 and Fig. S3) are similar and do not change this conclusion.

### Improved structures

In Figs. 10 and 13, it can be seen that the energies of the transition states in several cases are lower than those of the preceding or following intermediates (TS4 and TS7). This can happen when adding several corrections to the free energies, which have been obtained at different levels of theory. Small unbalances will frequently add up due to the mismatch in the potential surfaces. To minimize this effect with respect to the optimisations, we have recomputed the geometries of all intermediates and the key transition states at the B3LYP-D3/def2-TZVPD+COSMO ($\varepsilon = 80$) level of theory.

For most complexes, the geometries were qualitatively identical and only minor changes in the Mo-ligand distances were found, as can be seen in Tables S7 (DMDT) and S8 (MPT) in the supplementary material. However,

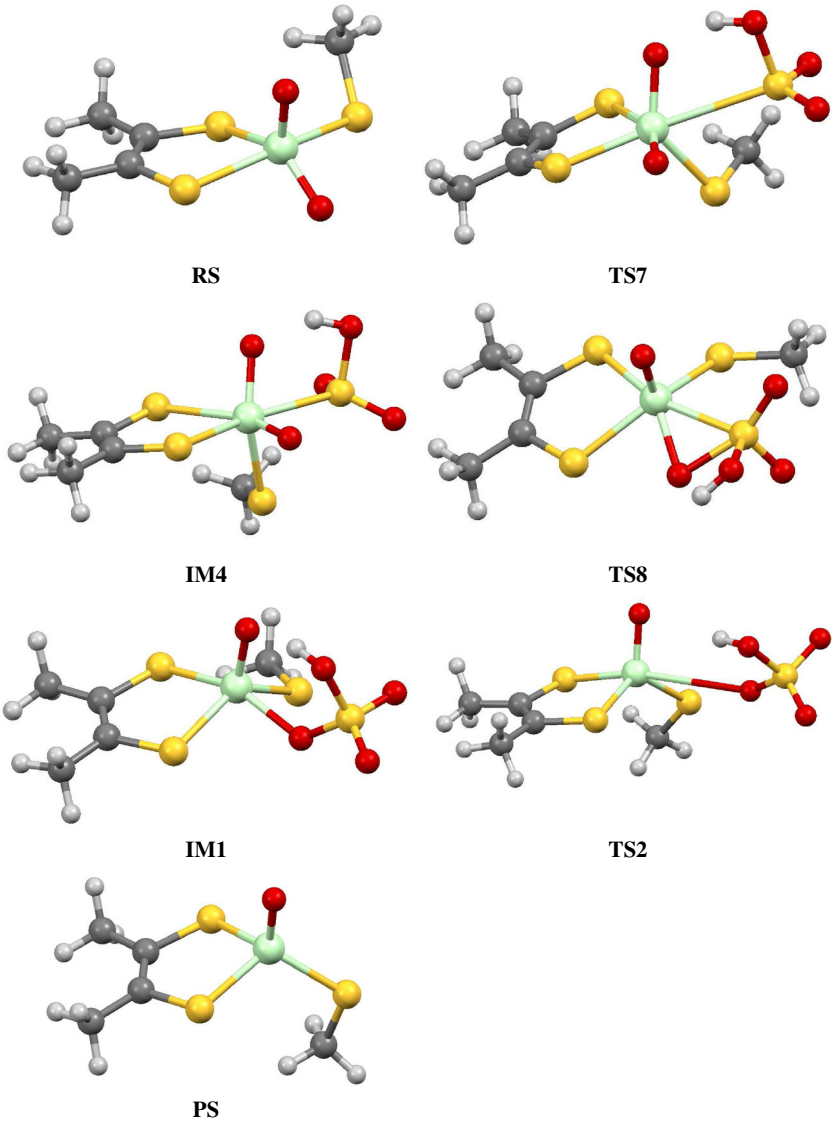


**Fig. 11** Optimized structures for the S→Mo mechanism using the model with DMDT and $HSO_3^-$

two intermediates could not be found at this level of theory: The first is IM3 for DMDT and the $SO_3^{2-}$ substrate. This is a serious discrepancy, because if the Mo–$OSO_2$ bond is broken before the new O–S bond is formed, it is no longer an O→Mo mechanism, but rather a S→OMo mechanism. Therefore, it indicates that the O→Mo mechanism is unlikely for DMDT and $SO_3^{2-}$, which is also supported by the large barrier observed with geometries obtained with the smaller basis set. On the other hand, the intermediate was still found with the more realistic MPT model, indicating that the mechanism is possible for the enzyme reaction, although it is high in energy.

Moreover, we could not find IM4 for any of the models with the $HSO_3^-$ substrate—instead the energy increased monotonously when the sulfur atom of $HSO_3^-$ approaches Mo. This is also serious, showing that the S→Mo mechanism can be discarded for this substrate—this mechanism requires the formation of a Mo–$SO_3H^-$ complex.

For the other mechanisms, we have calculated the reaction and activation energies at the B3LYP-D3/def2-TZVPD+COSMO ($\varepsilon = 80$) and LCCSD(T0) levels and compared to the same energies obtained with the original TPSS/def2-SV(P) structures. The differences in the calculated energies between the two sets of geometries are collected in Table S9. It can be seen that the change is not more than 20 kJ/mol at the LCCSD(T0) level and 34 kJ/mol at the DFT level, except for the MPT complexes with $SO_3^{2-}$ and the approximate TS8 structures. However, there are no qualitative differences between the two sets of structures and the observed differences do not change any of the general conclusions obtained in this paper.

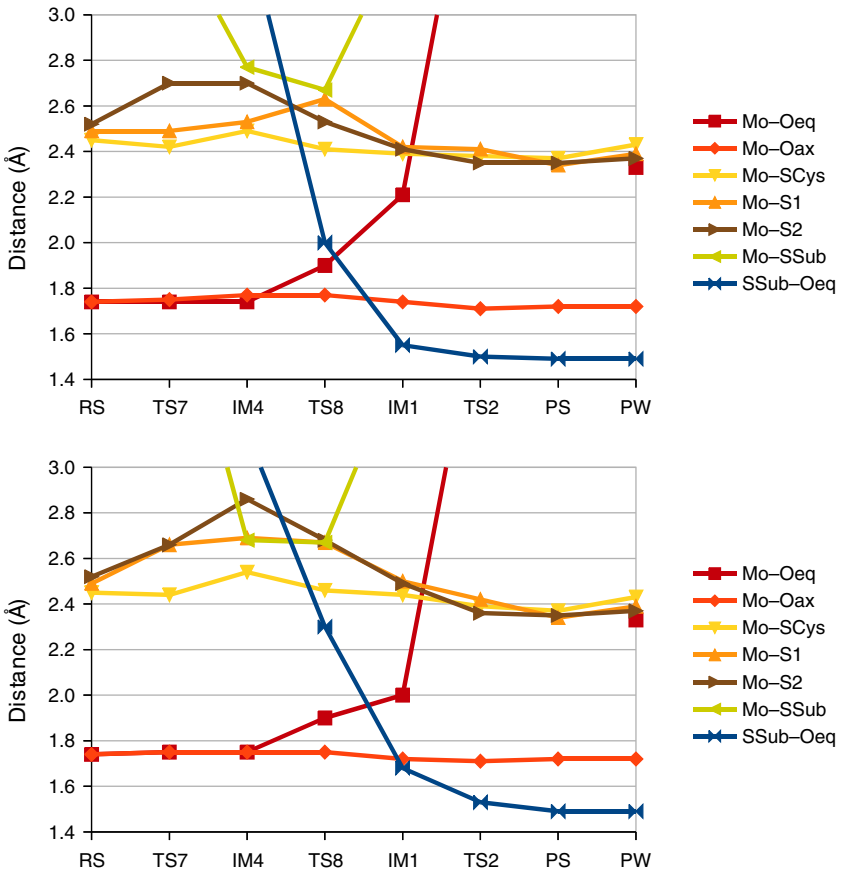


**Fig. 12** Important distances in the various reactants in the S→Mo mechanism with the MPT ligand and the **a** $HSO_3^-$ or **b** $SO_3^{2-}$ substrate. $S_1$ and $S_2$ are the two sulfur atoms of the MPT ligand ($S_1$ is cis to $O_{eq}$, whereas $S_2$ is cis to $S_{Cys}$

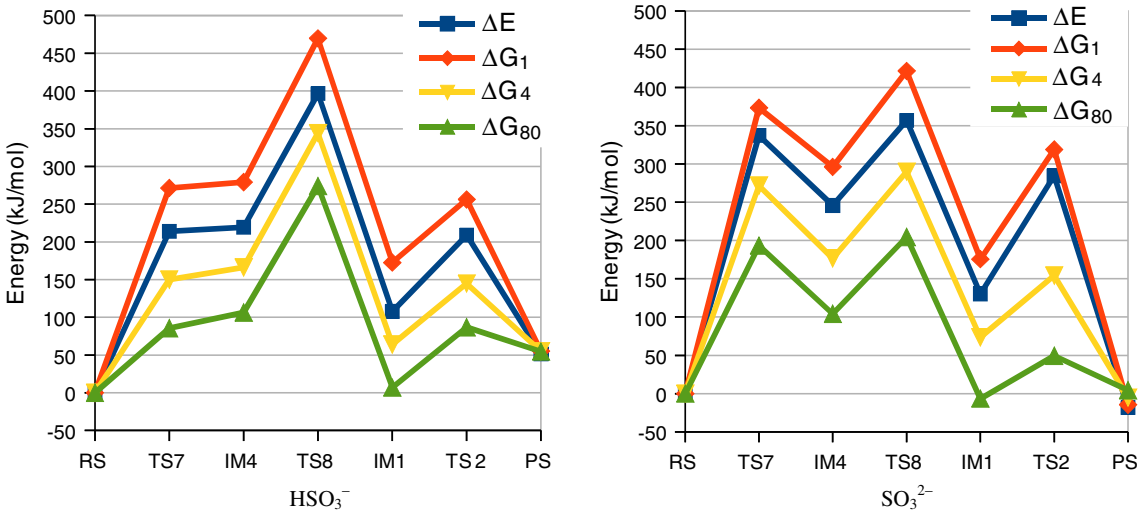


**Fig. 13** Energies for the S→Mo mechanism with MPT and $HSO_3^-$ (*left*) or $SO_3^{2-}$ (*right*; kJ/mol)

## Conclusions

In this paper, we have used QM cluster calculations to compare the three reaction mechanisms suggested for sulfite oxidase [13, 14], viz. the attack of $S_{Sub}$ on OMo, the attack of $O_{Sub}$ on Mo, or the attack of $S_{Sub}$ on Mo (Fig. 3). For the first time, these three mechanisms have been studied on an equal footing on the same small cluster models with the TPSS and B3LYP DFT methods and accurate LCCSD(T0) calculations. The reactions of two different substrates, $HSO_3^-$ and $SO_3^{2-}$, with two model systems for the active site of the sulfite oxidase enzyme,

$[MoO_2(DMDT)(SCH_3)]^-$ and $[MoO_2(MPT)(SCH_3)]^-$, were studied.

For the S→Mo mechanism, a complex of $SO_3^{2-}$ bound to Mo by the $S_{Sub}$ atom was obtained, but with the $HSO_3^-$ substrate and with a large basis set, this complex could not be found. Moreover, it was hard to continue this reaction without breaking the Mo–$S_{Sub}$ bond (leading to the S→OMo mechanism) and our approximate transition states were high in energy. Therefore, this mechanism can be ruled out.

For the O→Mo mechanism, the states suggested by Sarkar and coworkers [19] were initially investigated, but we could not find any reasonable path connecting these states—the rate-limiting transition state they present for this mechanism has a broken Mo–O bond and is very similar to our rate-limiting transition state of the S→OMo mechanism (TS1). Instead, we found the more complicated mechanism shown in Fig. 8, involving a bidentate sulfate complex, as well as for $HSO_3^-$ proton transfers to and back from the spectator $O_{ax}$ ligand. Moreover, this reaction path involves barriers that are higher than for the S→OMo mechanism by 30–57 kJ/mol for the sulfite-oxidase models.

Thus, the results presented here quite conclusively support the S→OMo mechanism. The reaction is simple, involving only a single Mo–sulfate intermediate and two transition states for the formation of the $S_{Sub}$–$O_{eq}$ bond and for the cleavage of the Mo–$O_{eq}$ bond (Fig. 5). The first transition state (TS1) involves the chemical step and the reduction of the Mo ion, and it is rate limiting.

The only remaining problem is that even for the preferred S→OMo mechanism, all calculated activation barriers are high, 107–159 kJ/mol, and are sensitive to the details of the calculations, in particular the dielectric constant of the continuum-solvation model. It is often observed that realistic results for protein calculations are obtained with dielectric constants of 2–20 [28, 29, 44, 45], but for charged groups in proteins, larger values are needed [72]. Moreover, it has been shown that for sites with many preorganized dipoles pointing toward the active site, the effective dielectric constant can actually be larger than 80 [73]. Therefore, it is not unexpected that the best barriers are obtained with the largest dielectric constant for sulfite oxidase, for which the active site is highly polar with many charged groups. The reason for the high activation barrier is that the reaction takes place between a negatively charged Mo complex (−1) and a negatively charged substrate (−1 or −2), giving rise to a large Coulomb repulsion between the two reactants. Most previous theoretical investigations with similar models have given similar barriers [19, 24, 25].

However, recently Hernandez-Marin and Ziegler [27] obtained appreciably lower and more reasonable barriers (29 and 61 kJ/mol for the TS1 and TS2) by adding a model of an Arg residue to the Mo model, neutralizing it and thereby avoiding the Coulombic barrier. Although this is an attractive approach, it is problematic, because the active site of sulfite oxidase actually contains four Arg residues within 10 Å from the Mo ion, three of which interact directly with the sulfate product in the crystal structure [8]. In addition, there are several other polar residues (Asp, His, Tyr, Trp) in the active site. Therefore, it is not obvious that inclusion of only one of these residues will give realistic reaction energies. Moreover, test calculations show that the results critically depend on the specific restraints that are applied on the Arg model and how the reference point of the reaction energies is defined (their reference state involved the substrate interacting with the Arg model, 4.9 Å from $O_{eq}$, not a free substrate as in our calculations). In our view, unbiased reaction energies can only be obtained if all active-site residues are included in the calculations, e.g. by a QM/MM approach. Efforts in that direction are in progress.

**Acknowledgments** This investigation has been supported by grants from the Swedish research council (project 2010-5025), from the Swedish Institute, the Crafoord Foundation, the National Basic Research Program of China (973 Program, 2012CB932800), the National Natural Science Foundation of China (NSFC 21103064), and from COST through Action CM1003. It has also been supported by computer resources of Lunarc at Lund University. The collaboration between the Universities of Lund and Göttingen has been carried out within the framework of the International Research Training Group "Metal Sites in Biomolecules—Structures, Regulation, Mechanisms" and M. A. is supported through a Ph.D. scholarship in this International Research Training Group.

## References

1. Kaim W, Schwederski B (1991) Bioinorganic chemistry: inorganic elements in the chemistry of life J. Wiley, Chichester
2. Hu YL, Ribbe MW (2010) Acc Chem Res 43:475
3. Hille R (1996) Chem Rev 96:2757
4. Mendel RR, Bittner F (2006) Biochim Biophys Acta 1763:621–663
5. Feng CJ, Tollin G, Enemark JH (2007) Biochim Biophys Acta 1774:527–539
6. Mendel RR (2007) J Exp Bot 58:2289–2296
7. Pilato RS, Stiefel EI (1999) Bioinorganic catalysis, 2nd edn (Reedijk J, Bouwman E eds) Marcel Dekker, New York, pp 81–152
8. Kisker C, Schindelin H, Pacheco A, Wehbi WA, Garrett RM, Rajagopalan KV, Enemark JH, Rees DC (1997) Cell 91:973–983
9. Schrader N, Fischer K, Theis K, Mendel RR, Schwarz G, Kisker C (2003) Structure 11:1251–1263
10. Kappler U, Bailey S (2005) J Biol Chem 280:24999–25007
11. Karakas E, Wilson HL, Graf TN, Xiang S, Jaramillo-Buswuets S, Rajagopalan KV, Kisker C (2005) J Biol Chem 280:33506–33515
12. Kappler U, Bailey S, Feng CJ, Honeychurch MJ, Hanson GR, Bernhardt PV, Tollin G, Enemark JH (2006) Biochemistry 45:9696–9705

13. Hille R (1994) Biochem Biophys Acta 1184:143
14. Hille R (1997) J Biol Inorg Chem 2:804
15. Das SK, Chaudhury PK, Biswas D, Sarkar S (1994) J Am Chem Soc 116:9061–9070
16. Chaudhury PK, Das SK, Sarkar S (1996) Biochem J 319:953–959
17. Lorber C, Plutino MR, Elding LI, Nordlander E (1997) J Chem Soc Dalton Trans 21:3997–4004
18. Nagarajan K, Chaudhury PK, Srinivasan BR, Sarkar S (2001) Chem Commun 1786–1787
19. Pal K, Chaudhury PK, Sarkar S (2007) Chem Asian J 2:956–964
20. George GN, Garrett RM, Graf T, Prince RC, Rajagopalan KV (1998) J Am Chem Soc 120:4522–4523
21. Klein EL, Raitsimring AM, Atashkin AV, Rajapakshe A, Johnson-Winters K, Arnold AR, Potapov A, Goldfarb D, Enemark JH (2012) Inorg Chem 51:1408–1418
22. Klein EL, Raitsimring AM, Atashkin AV, Enemark JH (2013) Coord Chem Rev 257:110–118
23. Astashkin AV, Johnson-Winters K, Klein EL, Feng CJ, Wilson HL, Rajagopalan KV, Raitsimring AK, Enemark JH (2008) J Am Chem Soc 130:8471–8480
24. Thapper A, Deeth RJ, Nordlander E (1999) Inorg Chem 38:1015–1018
25. Peariso K, McNaughton RL, Kirk M (2002) J Am Chem Soc 124:9006–9007
26. Majumdar A, Sarkar S (2011) Coord Chem Rev 255:1039–1054
27. Hernandez-Marin E, Ziegler T (2009) Inorg Chem 48:1323–1333
28. Siegbahn PEM, Borowski T (2006) Acc Chem Res 39:729–738
29. Siegbahn PEM, Himo F (2009) J Biol Inorg Chem 14:643–651
30. Li J-L, Mata RA, Ryde U (2013) J Chem Theory Comput 9:1799–1807
31. Liao R-Z, Thiel W (2012) J Chem Theory Comput 8:3793–3803
32. Liao R-Z, Thiel W (2013) J Comput Chem 34:2389–2397
33. Startk JG, Wallace HG (1982) Chemistry data book, p 74
34. Tao J, Perdew JP, Staroverov VN, Scuseria GE (2003) Phys Rev Lett 91:146401
35. Weigend F, Ahlrichs R (2005) Phys Chem Chem Phys 7:3297–3305
36. Eichkorn K, Treutler O, Öhm H, Häser M, Ahlrichs R (1995) Chem Phys Lett 240:283–290
37. Eichkorn K, Weigend F, Treutler O, Ahlrichs R (1997) Theor Chem Acc 97:119–126
38. Rappoport D, Furche F (2010) J Chem Phys 133:134105
39. Lee C, Yang W, Parr RG (1988) Phys Rev B 37:785
40. Becke AD (1993) J Chem Phys 98:5648
41. Klamt A, Schüürmann J (1993) J Chem Soc Perkin Trans 2(5):799–805
42. Schäfer A, Klamt A, Sattel D, Lohrenz JCW, Eckert F (2000) Phys Chem Chem Phys 2:2187–2193
43. Klamt A, Jonas V, Bürger T, Lohrenz JCW (1998) J Phys Chem 102:5074
44. Sharp KA (1990) Annu Rev Biophys Biophys Chem 19:301
45. Honig B (1995) Science 268:1144
46. Treutler O, Ahlrichs R (1995) J Chem Phys 102:346–354
47. Grimme S, Antony J, Ehrlich S, Krieg H (2010) J Chem Phys 132:154104
48. http://toc.uni-muenster.de/DFTD3/getd3.html. Accessed 18 June 2013
49. Miertus S, Scrocco E, Tomasi J (1981) Chem Phys 55:117
50. Tomasi J, Mennucci B, Cammi R (2005) Chem Rev 105:2999–3093
51. Frisch MJ, Trucks GW, Schlegel HB, Scuseria GE, Robb MA, Cheeseman JR, Montgomery Jr JA, Vreven T, Kudin KN, Burant JC, Millam JM, Iyengar SS, Tomasi J, Barone V, Mennucci B, Cossi M, Scalmani G, Rega N, Petersson GA, Nakatsuji H, Hada M, Ehara M, Toyota K, Fukuda R, Hasegawa J, Ishida M, Nakajima T, Honda Y, Kitao O, Nakai H, Klene M, Li X, Knox JE, Hratchian HP, Cross JB, Bakken V, Adamo C, Jaramillo J, Gomperts R, Stratmann RE, Yazyev O, Austin AJ, Cammi R, Pomelli C, Ochterski JW, Ayala PY, Morokuma K, Voth GA, Salvador P, Dannenberg JJ, Zakrzewski VG, Dapprich S, Daniels AD, Strain MC, Farkas O, Malick DK, Rabuck AD, Raghavachari K, Foresman JB, Ortiz JV, Cui Q, Baboul AG, Clifford S, Cioslowski J, Stefanov BB, Liu G, Liashenko A, Piskorz P, Komaromi I, Martin RL, Fox DJ, Keith T, Al-Laham MA, Peng CY, Nanayakkara A, Challacombe M, Gill PMW, Johnson B, Chen W, Wong MW, Gonzalez C, Pople JA Gaussian 03, revision D.01. Gaussian Inc., Wallingford
52. Ryde U, Mata RA, Grimme S (2011) Dalton Trans 40:11176–11183
53. Schütz M, Hetzer G, Werner H-J (1999) J Chem Phys 111:5691
54. Hampel C, Werner H-J (1996) J Chem Phys 104:6286
55. Kendall RA, Dunning TH, Harrison RJ (1992) J Chem Phys 96:6796
56. Dunning TH Jr (1989) J Chem Phys 90:1007–1023
57. Peterson KA, Figgen D, Dolg M, Stoll H (2007) J Chem Phys 126:124101
58. Polly R, Werner H-J, Manby FR, Knowles PJ (2004) Mol Phys 102:2311
59. Werner H-J, Manby FR, Knowles PJ (2003) J Chem Phys 118:8149
60. Weigend F (2002) Phys Chem Chem Phys 4:4285
61. Weigend F, Köhn A, Hättig C (2002) J Chem Phys 116:3175
62. Weigend F (2007) J Comput Chem 29:167
63. Weigend F, Häser M, Patzelt H, Ahlrichs R (1998) Chem Phys Lett 294:143
64. Pipek J, Mezey PG (1989) J Chem Phys 90:4916–4926
65. Mata RA, Werner H-J (2007) Mol Phys 105:2753–2761
66. Werner H-J, Knowles PJ, Knizia G, Manby FR, Schütz M et al (2012) Molpro, version 2012.1, a package of ab initio programs. see http://www.molpro.net
67. Helgaker T, Klopper W, Koch H, Noga J (1997) J Chem Phys 106:9639
68. Harris HH, George GN, Rajagopalan KV (2006) Inorg Chem 45:493–494
69. Amzel LM (1997) Proteins Struct Funct Genet 28:144
70. Rulíšek L, Jensen KP, Lundgren K, Ryde U (2006) J Comput Chem 27:1398–1414
71. Irudayam SJ, Henchman RH (2009) J Phys Chem B 113:5871–5884
72. Schutz CN, Warshel A (2001) Proteins 44:400–417
73. Ryde U (1996) Eur Biophys J 24:213–221